Acta Mechanica

Scattering of antiplane shear wave by a piezoelectric circular cylinder with an imperfect interface

X. Wang and **E. Pan**, Akron, Ohio, and **A. K. Roy**, WPAFB, Ohio

Summary. We present analytical solutions for the scattering of an antiplane shear wave by a piezoelectric circular cylinder with an imperfect interface. We first consider the simple case in which the imperfection is homogeneous along the interface. Two typical imperfect interfaces are addressed: 1) mechanically compliant and dielectrically weakly conducting interface, and 2) mechanically compliant and dielectrically highly conducting interface. The expressions for the directivity pattern and scattering cross-section of the scattered shear waves are derived. We then investigate the more difficult problem in which the imperfection is circumferentially inhomogeneous along the interface. A concise expression for an inhomogeneously compliant and weakly conducting interface is derived by means of matrix notation. Numerical examples are presented to demonstrate the effect of the imperfection and the circumferential inhomogeneity of the interface on the directivity patterns and scattering cross-sections of the scattered shear wave. The circumferentially inhomogeneous interface is also utilized to model the interface where an arbitrary number of cracks exist. Results show that when every part of the interface is rather compliant, large low-frequency peaks of the scattered cross-sections, which correspond to the resonance scattering, can be observed no matter if the interface is homogeneous or inhomogeneous. The appearance of large low-frequency peaks can be well explained by estimating the natural frequency of the corresponding reduced mass-spring system where the cylinder is assumed as a rigid body. Peaks of the scattered cross-sections spanning from low frequencies to high frequencies can be observed for a cylinder with a partially debonded interface.

1 Introduction

It is well known that due to possible manufacturing errors and preexisting microcracks/defects, damages in different degrees exist along the interface of composite materials. Therefore, to capture the effect of such a damaged interface on the field response, suitable imperfect interface models, instead of the perfect ones, need to be utilized, which renders the necessity of studying the mechanical behaviors of various imperfect interface models.

The static and dynamic behaviors of composites in the presence of imperfect interface have received considerable attention from researchers (see, for example, [1]–[8]). In continuum mechanics, an imperfect interface is primarily based on the assumption that tractions are continuous across the interface whilst the jumps in displacements across the interface are proportional to the respective interfacial tractions in terms of the "spring-type" interface parameters. The "imperfect interface" concept also exists in the fields of thermal conduction [9],

[10] and electrostatics [11]. While the static Green's functions associated with imperfect inter-faces were derived by Pan [12]–[15], the static behavior of piezoelectric composites with imperfect interface was addressed by Wang and Sudak [16]. Most recently, Fan et al. [17] found that certain waves exist which propagate near an imperfectly bonded interface between two half-spaces of different piezoelectric ceramics. In [17] the imperfect interface was modeled by the linear spring model [1]–[8] (or equivalently the so-called shear-lag model [18]).

The present research is further motivated by recent reports that the existence of a very compliant interphase layer between the fiber and the surrounding matrix could be the mech-anism for the photonic band gap (or the strong attenuation band) of the locally resonant sonic crystal [19]–[21]. As such our mechanically compliant and dielectrically weakly conducting (or highly conducting) interface with vanishing thickness is relevant (as explained later on). This interface model is also suitable to simulate a thin interphase layer of finite thickness between the piezoelectric cylinder and piezoelectric matrix.

This research is, therefore, devoted to the antiplane shear wave scattering by a piezoelectric circular cylinder of infinite length, which is imperfectly bonded to a piezoelectric matrix. The imperfect interface between the cylinder and matrix can be: 1) mechanically compliant and dielectrically weakly conducting, or 2) mechanically compliant and dielectrically highly con-ducting. As in Wang and Sudak [16], we adopt the aforementioned linear spring model to simulate a mechanically compliant interface. A dielectrically weakly conducting interface [9]–[11], [16] is based on the assumption that the normal electric displacement is continuous but the electric potential is discontinuous across the interface with its jump proportional to the normal electric displacement. On the other hand, a dielectrically highly conducting interface [10], [16], [22] is based on the premise that the electric potential is continuous across the interface whereas the normal electric displacement has a discontinuity across the interface, which is proportional to certain differential expressions of the electric potential. Both the simple circumferentially homogeneous and circumferentially inhomogeneous interfaces (see, e.g., [4] or [10] for details on the inhomogeneous interface model) are investigated in this paper. Furthermore, the inhomogeneous interface can be conveniently utilized to model the interface along which an arbitrary number of cracks exist.

Our analyses show that if the interface is homogeneous, then it is sufficient to invert a 2×2 matrix and an infinite number of 4×4 matrices to solve the involved unknowns. On the other hand, if the interface is circumferentially inhomogeneous, it requires that a simultaneous infi-nite system of linear algebraic equations be solved. Numerical examples are presented to demonstrate the influence of the interface imperfection and inhomogeneity on the directivity patterns and scattering cross-sections of the scattered shear wave. While our numerical results are from the forward solution algorithm, they have demonstrated clearly that the far-field scattering field can be significantly influenced by the interface imperfection. In other words, the induced field carries important information for the possible inverse of the interface geometry and mechanical/electric behaviors. This thus opens the new opportunity of designing imperfect interface for desirable band gaps [19]–[21].

2 Basic formulations

We consider an infinite long piezoelectric circular cylinder of radius R embedded in an unbounded piezoelectric matrix as shown in Fig. 1. The region occupied by the cylinder is $S_1 : x^2 + y^2 \leq R^2$ and that by the matrix is $S_2 : x^2 + y^2 \geq R^2$. The cylinder and matrix are both
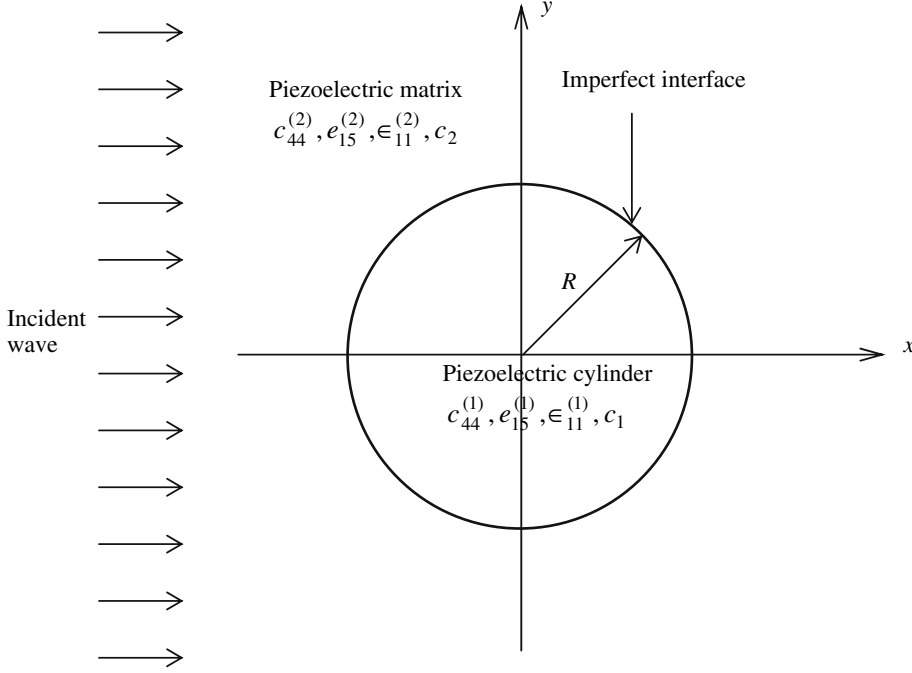
Fig. 1. An infinite long piezoelectric circular cylinder embedded in an infinite piezoelectric matrix (cross-section view at $z = $ constant)

transversely isotropic with their poling direction parallel to the z-axis. The cylinder is subject to an incident antiplane shear wave traveling in the positive x-direction. Throughout the paper, the superscripts (1) and (2) (or the subscripts 1 and 2) are used to identify the corresponding quantities in the cylinder and matrix, respectively. In addition, the time factor $e^{-i\omega t}$, where ω is the angular frequency, is suppressed.

For the problem considered, the linear piezoelectric constitutive equations in a polar coordinate system are given by

$$\sigma_{zr} = c_{44}\frac{\partial w}{\partial r} + e_{15}\frac{\partial \phi}{\partial r}, \quad D_r = e_{15}\frac{\partial w}{\partial r} - \in_{11}\frac{\partial \phi}{\partial r},$$

$$\sigma_{z\theta} = c_{44}\frac{\partial w}{r\partial \theta} + e_{15}\frac{\partial \phi}{r\partial \theta}, \quad D_\theta = e_{15}\frac{\partial w}{r\partial \theta} - \in_{11}\frac{\partial \phi}{r\partial \theta}, \tag{1}$$

where σ_{zr} and $\sigma_{z\theta}$ are the stress components; D_r and D_θ are the electric displacement components; w and ϕ are, respectively, the out-of-plane displacement and electric potential; c_{44}, e_{15}, and $\in_{11}$ are, respectively, the elastic modulus, piezoelectric coefficient, and dielectric permittivity. In addition, w and ϕ satisfy the following coupled partial differential equations:

$$c_{44}\nabla^2 w + \rho\omega^2 w + e_{15}\nabla^2\phi = 0,$$

$$e_{15}\nabla^2 w - \in_{11}\nabla^2\phi = 0, \tag{2}$$

where ∇^2 is the two-dimensional Laplace operator and ρ the mass density of the piezoelectric material.

We then introduce a new function φ which is related to w and ϕ via

$$\varphi = \phi - \frac{e_{15}}{\in_{11}}w. \tag{3}$$

As a result, Eq. (2) is decoupled into

$$\nabla^2 w + k^2 w = 0,$$

$$\nabla^2 \varphi = 0,$$

(4)

where $k = \frac{\omega}{c}$, $c = \sqrt{\frac{\tilde{c}_{44}}{\rho}}$, with $\tilde{c}_{44} = c_{44} + \frac{e_{15}^2}{\in_{11}}$ being the piezoelectrically stiffened elastic constant and c the shear wave speed. Meanwhile, the stress and electric displacement components can be expressed in terms of w and φ as

$$\sigma_{zr} = \tilde{c}_{44} \frac{\partial w}{\partial r} + e_{15} \frac{\partial \varphi}{\partial r}, \quad D_r = -\in_{11} \frac{\partial \varphi}{\partial r},$$

$$\sigma_{z\theta} = \tilde{c}_{44} \frac{\partial w}{r\partial \theta} + e_{15} \frac{\partial \varphi}{r\partial \theta}, \quad D_\theta = -\in_{11} \frac{\partial \varphi}{r\partial \theta}.$$

(5)

The interface between the cylinder and matrix is first assumed to be homogeneously imperfect. Furthermore, two typical imperfect interfaces are considered in this paper: 1) a mechanically compliant and dielectrically weakly conducting interface; 2) a mechanically compliant and dielectrically highly conducting interface. According to the definitions described in the Introduction, the boundary conditions on a mechanically compliant and dielectrically weakly conducting interface $r = R$ can be expressed as

$$\sigma_{zr}^{(1)} = \sigma_{zr}^{(2)} = \alpha(w^{(2)} - w^{(1)}), \quad D_r^{(1)} = D_r^{(2)} = -\beta(\phi^{(2)} - \phi^{(1)}), \quad r = R,$$

(6)

where the two interface parameters α and β are nonnegative constants. The case where $\alpha, \beta \to \infty$ corresponds to a perfect interface, whereas $\alpha = \beta = 0$ describes a completely debonded and charge-free (insulating) interface.

The boundary conditions on a mechanically compliant and dielectrically highly conducting interface $r = R$ can be expressed as

$$\sigma_{zr}^{(1)} = \sigma_{zr}^{(2)} = \alpha(w^{(2)} - w^{(1)}), \quad \phi^{(1)} = \phi^{(2)}, \quad \frac{1}{r^2} \frac{\partial^2 \phi^{(1)}}{\partial \theta^2} = \gamma(D_r^{(2)} - D_r^{(1)}), \quad r = R,$$

(7)

where γ is a nonnegative constant. The case where $\alpha, \gamma \to \infty$ corresponds to a perfect interface, whereas $\alpha = \gamma = 0$ describes a completely debonded and equipotential interface.

In view of Eqs. (3) and (5), Eq. (6) can also be expressed in terms of w and φ as

$$\tilde{c}_{44}^{(1)} \frac{\partial w^{(1)}}{\partial r} + e_{15}^{(1)} \frac{\partial \varphi^{(1)}}{\partial r} = \tilde{c}_{44}^{(2)} \frac{\partial w^{(2)}}{\partial r} + e_{15}^{(2)} \frac{\partial \varphi^{(2)}}{\partial r} = \alpha(w^{(2)} - w^{(1)}),$$

$$\in_{11}^{(1)} \frac{\partial \varphi^{(1)}}{\partial r} = \in_{11}^{(2)} \frac{\partial \varphi^{(2)}}{\partial r} = \beta \left[\varphi^{(2)} - \varphi^{(1)} + \frac{e_{15}^{(2)}}{\in_{11}^{(2)}} w^{(2)} - \frac{e_{15}^{(1)}}{\in_{11}^{(1)}} w^{(1)} \right], \quad r = R,$$

(8)

and Eq. (7) in terms of w and φ as

$$\tilde{c}_{44}^{(1)} \frac{\partial w^{(1)}}{\partial r} + e_{15}^{(1)} \frac{\partial \varphi^{(1)}}{\partial r} = \tilde{c}_{44}^{(2)} \frac{\partial w^{(2)}}{\partial r} + e_{15}^{(2)} \frac{\partial \varphi^{(2)}}{\partial r} = \alpha(w^{(2)} - w^{(1)}),$$

$$\varphi^{(1)} + \frac{e_{15}^{(1)}}{\in_{11}^{(1)}} w^{(1)} = \varphi^{(2)} + \frac{e_{15}^{(2)}}{\in_{11}^{(2)}} w^{(2)},$$

$$\frac{\partial^2 \varphi^{(1)}}{\partial \theta^2} + \frac{e_{15}^{(1)}}{\in_{11}^{(1)}} \frac{\partial^2 w^{(1)}}{\partial \theta^2} = \gamma R^2 \left(\in_{11}^{(1)} \frac{\partial \varphi^{(1)}}{\partial r} - \in_{11}^{(2)} \frac{\partial \varphi^{(2)}}{\partial r} \right), \quad r = R.$$

(9)

3 Solutions in terms of series expansion

Functions $w^{(1)}, \varphi^{(1)}$ in the cylinder and $w^{(2)}, \varphi^{(2)}$ in the matrix can be expanded in terms of $\cos(n\theta)$ as

$$
\left.\begin{aligned}
w^{(1)} &= A_0^{(1)} J_0(k_1 r) + \sum_{n=1}^{+\infty} A_n^{(1)} J_n(k_1 r) \cos(n\theta), \\
\varphi^{(1)} &= B_0^{(1)} + \sum_{n=1}^{+\infty} B_n^{(1)} r^n \cos(n\theta),
\end{aligned}\right\} \quad 0 \le r \le R,
\tag{10}
$$

$$
\left.\begin{aligned}
w^{(2)} &= e^{ik_2 x} + A_0^{(2)} H_0^{(1)}(k_2 r) + \sum_{n=1}^{+\infty} A_n^{(2)} H_n^{(1)}(k_2 r) \cos(n\theta), \\
\varphi^{(2)} &= \sum_{n=1}^{+\infty} B_n^{(2)} r^{-n} \cos(n\theta),
\end{aligned}\right\} \quad r \ge R,
\tag{11}
$$

where the first term $e^{ik_2 x}$ in $w^{(2)}$ is the incident antiplane shear wave (or incident SH wave) of the unit amplitude propagating along the positive x-direction, whilst $A_0^{(2)} H_0^{(1)}(k_2 r) + \sum_{n=1}^{+\infty} A_n^{(2)} H_n^{(1)}(k_2 r) \cos(n\theta)$ in $w^{(2)}$ is associated with the scattered shear wave from the cylinder; $H_n^{(1)}$ and J_n are the nth order Hankel and Bessel functions of the first kind, and $A_0^{(1)}, B_0^{(1)}, A_0^{(2)}, A_n^{(1)}, B_n^{(1)}, A_n^{(2)}, B_n^{(2)} (n = 1, 2, 3, \ldots, +\infty)$ are unknown constants to be determined.

In addition, the term $e^{ik_2 x}$ can be expanded as [23]

$$
e^{ik_2 x} = J_0(k_2 r) + 2\sum_{n=1}^{+\infty} i^n J_n(k_2 r) \cos(n\theta),
\tag{12}
$$

For a mechanically compliant and dielectrically weakly conducting interface, we enforce the boundary conditions (8) and solve the unknown expansion coefficients as

$$
\begin{bmatrix} A_0^{(1)} \\ A_0^{(2)} \end{bmatrix} = \begin{bmatrix} k_1 \tilde{c}_{44}^{(1)} J_1(k_1 R) & -k_2 \tilde{c}_{44}^{(2)} H_1^{(1)}(k_2 R) \\ k_1 \tilde{c}_{44}^{(1)} J_1(k_1 R) - \alpha J_0(k_1 R) & \alpha H_0^{(1)}(k_2 R) \end{bmatrix}^{-1} \begin{bmatrix} k_2 \tilde{c}_{44}^{(2)} J_1(k_2 R) \\ -\alpha J_0(k_2 R) \end{bmatrix},
$$

$$
B_0^{(1)} = \frac{e_{15}^{(2)}}{\in_{11}^{(2)}} J_0(k_2 R) + \begin{bmatrix} -\frac{e_{15}^{(1)}}{\in_{11}^{(1)}} J_0(k_1 R) & \frac{e_{15}^{(2)}}{\in_{11}^{(2)}} H_0^{(1)}(k_2 R) \end{bmatrix} \begin{bmatrix} A_0^{(1)} \\ A_0^{(2)} \end{bmatrix},
\tag{13}
$$

$$
\begin{bmatrix} A_n^{(1)} \\ B_n^{(1)} \\ A_n^{(2)} \\ B_n^{(2)} \end{bmatrix} = 2i^n \begin{bmatrix} k_1 \tilde{c}_{44}^{(1)} J_n'(k_1 R) & n e_{15}^{(1)} R^{n-1} & -k_2 \tilde{c}_{44}^{(2)} H_n^{(1)'}(k_2 R) & n e_{15}^{(2)} R^{-n-1} \\ k_1 \tilde{c}_{44}^{(1)} J_n'(k_1 R) + \alpha J_n(k_1 R) & n e_{15}^{(1)} R^{n-1} & -\alpha H_n^{(1)}(k_2 R) & 0 \\ 0 & \in_{11}^{(1)} R^{n-1} & 0 & \in_{11}^{(2)} R^{-n-1} \\ \beta \frac{e_{15}^{(1)}}{\in_{11}^{(1)}} J_n(k_1 R) & n \in_{11}^{(1)} R^{n-1} + \beta R^n & -\beta \frac{e_{15}^{(2)}}{\in_{11}^{(2)}} H_n^{(1)}(k_2 R) & -\beta R^{-n} \end{bmatrix}^{-1}
$$

$$
\times \begin{bmatrix} k_2 \tilde{c}_{44}^{(2)} J_n'(k_2 R) \\ \alpha J_n(k_2 R) \\ 0 \\ \beta \frac{e_{15}^{(2)}}{\in_{11}^{(2)}} J_n(k_2 R) \end{bmatrix}, \quad (n = 1, 2, 3, \ldots, +\infty),
$$

where the prime ($'$) denotes the derivative with respect to the variable in the parenthesis.

Similarly, for a mechanically compliant and dielectrically highly conducting interface, we enforce the boundary conditions (9) and find the unknowns to be

$$
\begin{bmatrix} A_0^{(1)} \\ A_0^{(2)} \end{bmatrix} = \begin{bmatrix} k_1 \tilde{c}_{44}^{(1)} J_1(k_1 R) & -k_2 \tilde{c}_{44}^{(2)} H_1^{(1)}(k_2 R) \\ k_1 \tilde{c}_{44}^{(1)} J_1(k_1 R) - \alpha J_0(k_1 R) & \alpha H_0^{(1)}(k_2 R) \end{bmatrix}^{-1} \begin{bmatrix} k_2 \tilde{c}_{44}^{(2)} J_1(k_2 R) \\ -\alpha J_0(k_2 R) \end{bmatrix},
$$

$$
B_0^{(1)} = \frac{e_{15}^{(2)}}{\in_{11}^{(2)}} J_0(k_2 R) + \begin{bmatrix} -\dfrac{e_{15}^{(1)}}{\in_{11}^{(1)}} J_0(k_1 R) & \dfrac{e_{15}^{(2)}}{\in_{11}^{(2)}} H_0^{(1)}(k_2 R) \end{bmatrix} \begin{bmatrix} A_0^{(1)} \\ A_0^{(2)} \end{bmatrix},
$$

(15)

$$
\begin{bmatrix} A_n^{(1)} \\ B_n^{(1)} \\ A_n^{(2)} \\ B_n^{(2)} \end{bmatrix} = 2\mathrm{i}^n \begin{bmatrix} k_1 \tilde{c}_{44}^{(1)} J_n'(k_1 R) & n e_{15}^{(1)} R^{n-1} & -k_2 \tilde{c}_{44}^{(2)} H_n^{(1)'}(k_2 R) & n e_{15}^{(2)} R^{-n-1} \\ k_1 \tilde{c}_{44}^{(1)} J_n'(k_1 R) + \alpha J_n(k_1 R) & n e_{15}^{(1)} R^{n-1} & -\alpha H_n^{(1)}(k_2 R) & 0 \\ \dfrac{e_{15}^{(1)}}{\in_{11}^{(1)}} J_n(k_1 R) & R^n & -\dfrac{e_{15}^{(2)}}{\in_{11}^{(2)}} H_n^{(1)}(k_2 R) & -R^{-n} \\ n\dfrac{e_{15}^{(1)}}{\in_{11}^{(1)}} J_n(k_1 R) & nR^n + \gamma \in_{11}^{(1)} R^{n+1} & 0 & \gamma \in_{11}^{(2)} R^{-n+1} \end{bmatrix}^{-1}
$$

$$
\times \begin{bmatrix} k_2 \tilde{c}_{44}^{(2)} J_n'(k_2 R) \\ \alpha J_n(k_2 R) \\ \dfrac{e_{15}^{(2)}}{\in_{11}^{(2)}} J_n(k_2 R) \\ 0 \end{bmatrix}, \quad (n = 1, 2, 3, \ldots, +\infty).
$$

(16)

4 Directivity pattern and scattering cross section

In the far field $r \to \infty$, the scattered component in w exhibits the following asymptotic behavior

$$
w^{(2s)} = \sqrt{\frac{2}{\pi k_2 r}} e^{\mathrm{i}\left(k_2 r - \frac{\pi}{4}\right)} \left[A_0^{(2)} + \sum_{n=1}^{+\infty} A_n^{(2)} e^{-\mathrm{i}\frac{n\pi}{2}} \cos(n\theta) \right], \quad r \to \infty,
$$

(17)

where the superscript (2s) indicates that this quantity is the scattering field in material 2, i.e., in the matrix.

As a result the electric potential $\phi^{(2)}$ and stress component $\sigma_{zr}^{(2)}$ in the far field induced by the scattered shear wave are

$$
\phi^{(2s)} = \frac{e_{15}^{(2)}}{\in_{11}^{(2)}} w^{(2s)}, \quad \sigma_{zr}^{(2s)} = \mathrm{i} k_2 \tilde{c}_{44}^{(2)} w^{(2s)}, \quad r \to \infty.
$$

(18)

It is observed from Eq. (18) that in the far field $\phi^{(2s)}$ is proportional to $w^{(2s)}$ and $\sigma_{zr}^{(2)}$. Therefore, the far field behaviors of the stress and elastic displacement in the piezoelectric matrix can be determined by the electric potential at the far field. The far-field directivity

pattern of scattering is defined as the plot exhibiting the angular distribution of the absolute value of the amplitude of the stress component $\sigma_{zr}^{(2)}$ at a large distance from the scatterer (i.e., the cylinder in this paper). Thus the directivity pattern of the scattered shear wave is given by [8], [24]

$$D(\theta) = \left| A_0^{(2)} + \sum_{n=1}^{+\infty} A_n^{(2)} e^{-\mathrm{i}\frac{n\pi}{2}} \cos(n\theta) \right|. \tag{19}$$

According to Liu et al. [24], the scattering cross-section of one scatterer is defined as the ratio of the total energy flow carried outwards by the scattered wave to the energy flow of the incident wave through a normal area that is equal to the cross-section area of the scatterer. Thus, the scattering cross-section of the shear wave for the cylinder is

$$Q = \frac{2\left| A_0^{(2)} \right|^2 + \sum_{n=1}^{+\infty} \left| A_n^{(2)} \right|^2}{k_2 R}. \tag{20}$$

5 Inhomogeneous interface

If the imperfection of the interface is not uniform but circumferentially inhomogeneous, then Eqs. (8) and (9) for the boundary conditions on the imperfect interface should be modified (see [10] for more details) to account for the nonuniformity of imperfection along the interface. As an example, in this section we only consider an inhomogeneously compliant and weakly conducting interface. It is noted that Eq. (8) is still valid here if we take α and β as functions of the circumferential angle θ, i.e., $\alpha = \alpha(\theta) \geq 0$ and $\beta = \beta(\theta) \geq 0$. However, in order to analyze the inhomogeneous imperfection along the interface, it is more feasible to expand $w^{(1)}, \varphi^{(1)}$ in the cylinder and $w^{(2)}, \varphi^{(2)}$ in the matrix, in terms of $e^{\mathrm{i}n\theta}$, as follows:

$$\left. \begin{aligned} w^{(1)} &= \sum_{n=-\infty}^{+\infty} A_n^{(1)} J_n(k_1 r) e^{\mathrm{i}n\theta}, \\ \varphi^{(1)} &= \sum_{n=-\infty}^{+\infty} B_n^{(1)} r^{|n|} e^{\mathrm{i}n\theta}, \end{aligned} \right\} \quad 0 \leq r \leq R, \tag{21}$$

$$\left. \begin{aligned} w^{(2)} &= e^{\mathrm{i}k_2 x} + \sum_{n=-\infty}^{+\infty} A_n^{(2)} H_n^{(1)}(k_2 r) e^{\mathrm{i}n\theta}, \\ \varphi^{(2)} &= \sum_{n=-\infty}^{+\infty} B_n^{(2)} r^{-|n|} e^{\mathrm{i}n\theta}, \end{aligned} \right\} \quad r \geq R, \tag{22}$$

where $A_n^{(1)}, B_n^{(1)}, A_n^{(2)}, B_n^{(2)}$ are unknown expansion coefficients to be determined. In addition, the term $e^{\mathrm{i}k_2 x}$ can be expanded as [23]

$$e^{\mathrm{i}k_2 x} = \sum_{n=-\infty}^{+\infty} \mathrm{i}^n J_n(k_2 r) e^{\mathrm{i}n\theta}. \tag{23}$$

The two given imperfect functions $\alpha(\theta)$ and $\beta(\theta)$, which are periodic functions of θ, can be expanded into the following two Fourier series:

$$\alpha(\theta) = \sum_{n=-\infty}^{+\infty} X_n e^{in\theta}, \quad \beta(\theta) = \sum_{n=-\infty}^{+\infty} Y_n e^{in\theta}, \tag{24}$$

where $X_{-n} = \bar{X}_n, \quad Y_{-n} = \bar{Y}_n \quad (n = 0, 1, 2, \ldots, +\infty)$ are known coefficients.

By enforcing the boundary conditions on the imperfect interface, we finally arrive at a set of linear algebraic equations for the expansion coefficients

$$k_1 \tilde{c}_{44}^{(1)} J_n'(k_1 R) A_n^{(1)} + |n| e_{15}^{(1)} R^{|n|-1} B_n^{(1)} - k_2 \tilde{c}_{44}^{(2)} H_n^{(1)'}(k_2 R) A_n^{(2)}$$
$$+ |n| e_{15}^{(2)} R^{-|n|-1} B_n^{(2)} = k_2 \tilde{c}_{44}^{(2)} i^n J_n'(k_2 R), \tag{25.1}$$

$$k_1 \tilde{c}_{44}^{(1)} J_n'(k_1 R) A_n^{(1)} + \sum_{m=-\infty}^{+\infty} X_{n-m} J_m(k_1 R) A_m^{(1)}$$
$$+ |n| e_{15}^{(1)} R^{|n|-1} B_n^{(1)} - \sum_{m=-\infty}^{+\infty} X_{n-m} H_m^{(1)}(k_2 R) A_m^{(2)} = \sum_{m=-\infty}^{+\infty} X_{n-m} i^m J_m(k_2 R), \tag{25.2}$$

$$|n| \in_{11}^{(1)} R^{|n|-1} B_n^{(1)} + |n| \in_{11}^{(2)} R^{-|n|-1} B_n^{(2)} = 0, \tag{25.3}$$

$$\frac{e_{15}^{(1)}}{\in_{11}^{(1)}} \sum_{m=-\infty}^{+\infty} Y_{n-m} J_m(k_1 R) A_m^{(1)} + |n| \in_{11}^{(1)} R^{|n|-1} B_n^{(1)} + \sum_{m=-\infty}^{+\infty} Y_{n-m} R^{|m|} B_m^{(1)}$$
$$- \frac{e_{15}^{(2)}}{\in_{11}^{(2)}} \sum_{m=-\infty}^{+\infty} Y_{n-m} H_m^{(1)}(k_2 R) A_m^{(2)} - \sum_{m=-\infty}^{+\infty} Y_{n-m} R^{-|m|} B_m^{(2)} = \frac{e_{15}^{(2)}}{\in_{11}^{(2)}} \sum_{m=-\infty}^{+\infty} Y_{n-m} i^m J_m(k_2 R), \tag{25.4}$$

where n is any integer from $-\infty$ to $+\infty$.

If we introduce the following vectors (as in [8] and [25]):

$$\mathbf{A}_1 = \left[A_n^{(1)} \right], \quad \mathbf{A}_2 = \left[A_n^{(2)} \right], \quad \mathbf{B}_1 = \left[B_n^{(1)} \right], \quad \mathbf{B}_2 = \left[B_n^{(2)} \right],$$

$$\mathbf{K}_1 = k_2 \tilde{c}_{44}^{(2)} \left[i^n J_n'(k_2 R) \right], \quad \mathbf{K}_2 = \left[\sum_{m=-\infty}^{+\infty} X_{n-m} i^m J_m(k_2 R) \right], \quad \mathbf{K}_4 = \frac{e_{15}^{(2)}}{\in_{11}^{(2)}} \left[\sum_{m=-\infty}^{+\infty} Y_{n-m} i^m J_m(k_2 R) \right], \tag{26}$$

and further define the following square matrices (as in [8] and [25]):

$$\mathbf{Q}_{11} = k_1 \tilde{c}_{44}^{(1)} \mathrm{diag} J_n'(k_1 R), \quad \mathbf{Q}_{12} = e_{15}^{(1)} \mathrm{diag} |n| R^{|n|-1},$$

$$\mathbf{Q}_{13} = -k_2 \tilde{c}_{44}^{(2)} \mathrm{diag} H_n^{(1)'}(k_2 R), \quad \mathbf{Q}_{14} = e_{15}^{(2)} \mathrm{diag} |n| R^{-|n|-1},$$

$$\mathbf{Q}_{21} = k_1 \tilde{c}_{44}^{(1)} \mathrm{diag} J_n'(k_1 R) + \left[X_{n-m} J_m(k_1 R) \right], \quad \mathbf{Q}_{22} = e_{15}^{(1)} \mathrm{diag} |n| R^{|n|-1}, \quad \mathbf{Q}_{23} = - \left[X_{n-m} H_m^{(1)}(k_2 R) \right],$$

$$\mathbf{Q}_{32} = \in_{11}^{(1)} \mathrm{diag} R^{|n|-1}, \quad \mathbf{Q}_{34} = \in_{11}^{(2)} \mathrm{diag} R^{-|n|-1}, \quad \mathbf{Q}_{41} = \frac{e_{15}^{(1)}}{\in_{11}^{(1)}} \left[Y_{n-m} J_m(k_1 R) \right],$$

$$\mathbf{Q}_{42} = \in_{11}^{(1)} \mathrm{diag} |n| R^{|n|-1} + \left[Y_{n-m} R^{|m|} \right], \quad \mathbf{Q}_{43} = -\frac{e_{15}^{(2)}}{\in_{11}^{(2)}} \left[Y_{n-m} H_m^{(1)}(k_2 R) \right], \quad \mathbf{Q}_{44} = - \left[Y_{n-m} R^{-|m|} \right], \tag{27}$$

then the original set of linear algebraic equations (25) can be equivalently expressed as

Table 1. Material properties of BaTiO$_3$ and PZT-5

	c_{44} (10^{10} N/m^2)	$\tilde{c}_{44}$ (10^{10} N/m^2)	e_{15} (C/m^2)	$\in_{11}$ (10^{-9} F/m)	ρ (10^3 kg/m^3)	c(m/s)
BaTiO$_3$	4.4	5.7164	11.4	9.8722	5.7	3166.8
PZT-5	2.11	3.9754	12.3	8.1103	7.75	2264.9

$$\begin{bmatrix} \mathbf{Q}_{11} & \mathbf{Q}_{12} & \mathbf{Q}_{13} & \mathbf{Q}_{14} \\ \mathbf{Q}_{21} & \mathbf{Q}_{22} & \mathbf{Q}_{23} & \mathbf{0} \\ \mathbf{0} & \mathbf{Q}_{32} & \mathbf{0} & \mathbf{Q}_{34} \\ \mathbf{Q}_{41} & \mathbf{Q}_{42} & \mathbf{Q}_{43} & \mathbf{Q}_{44} \end{bmatrix} \begin{bmatrix} \mathbf{A}_1 \\ \mathbf{B}_1 \\ \mathbf{A}_2 \\ \mathbf{B}_2 \end{bmatrix} = \begin{bmatrix} \mathbf{K}_1 \\ \mathbf{K}_2 \\ \mathbf{0} \\ \mathbf{K}_4 \end{bmatrix}, \tag{28}$$

with its solution being given by

$$\begin{bmatrix} \mathbf{A}_1 \\ \mathbf{B}_1 \\ \mathbf{A}_2 \\ \mathbf{B}_2 \end{bmatrix} = \begin{bmatrix} \mathbf{Q}_{11} & \mathbf{Q}_{12} & \mathbf{Q}_{13} & \mathbf{Q}_{14} \\ \mathbf{Q}_{21} & \mathbf{Q}_{22} & \mathbf{Q}_{23} & \mathbf{0} \\ \mathbf{0} & \mathbf{Q}_{32} & \mathbf{0} & \mathbf{Q}_{34} \\ \mathbf{Q}_{41} & \mathbf{Q}_{42} & \mathbf{Q}_{43} & \mathbf{Q}_{44} \end{bmatrix}^{-1} \begin{bmatrix} \mathbf{K}_1 \\ \mathbf{K}_2 \\ \mathbf{0} \\ \mathbf{K}_4 \end{bmatrix}. \tag{29}$$

Apparently if the interface is inhomogeneously imperfect, one needs to solve a simultaneous infinite system of linear algebraic equations to find the unknowns (see Eq. (28)). This is different to the uniform interface case where it is sufficient to invert a 2×2 matrix and an infinite number of 4×4 matrices to find the involved unknowns (see Eqs. (13)–(16)).

The directivity pattern of the scattered shear wave is now given by

$$D(\theta) = \left| \sum_{n=-\infty}^{+\infty} A_n^{(2)} e^{in\left(\theta - \frac{\pi}{2}\right)} \right|, \tag{30}$$

and the scattering cross-section of the shear wave for the cylinder is

$$Q = \frac{2}{k_2 R} \sum_{n=-\infty}^{+\infty} \left| A_n^{(2)} \right|^2. \tag{31}$$

6 Examples

In the following two subsections we will consider a PZT-5 cylinder imperfectly bonded to a BaTiO$_3$ matrix by a uniform interface (Subsect. 6.1) or by a circumferentially inhomogeneous interface (Subsect. 6.2). The material properties of BaTiO$_3$ and PZT-5 are listed in Table 1.

6.1 A uniform interface

In this subsection we consider a uniform interface. In our calculation, the series in Eqs. (10) and (11) are truncated at $n = N$ to obtain the results with a relative error less than 1%. Table 2 demonstrates the dependence of N on frequency $k_1 R$. It is observed that N is a monotonically

Table 2. Dependence of truncation number N on frequency k_1R

k_1R	0.5	1	5	10	20	40	80	120	160	200	300	400	500	600	1000
N	2	2	6	10	18	36	66	98	126	156	230	300	376	444	734

increasing function of k_1R . On the other hand, our calculations show that N is independent of the degree of the interface imperfection.

Figure 2 shows the directivity patterns of the scattered waves for a perfectly bonded ($\alpha, \beta \to \infty$ or $\alpha, \gamma \to \infty$) cylinder for eight different frequencies $k_1R = 0.5, 1, 5, 10, 20, 40, 80, 120$. Figures 3 and 4 plot, respectively, the corresponding results for a compliant and weakly conducting interface with $\alpha = 0.1\frac{\mu_1}{R}$, $\beta = 0.1\frac{\in_1}{R}$ and those for a compliant and highly conducting interface with $\alpha = 0.1\frac{\mu_1}{R}$, $\gamma = \frac{0.1}{\in_1 R}$, with $\alpha = 0.1\frac{\mu_1}{R}$ representing a rather compliant interface. It is observed from Figs. 2–4 that 1) with increasing frequency, the directivity pattern becomes complicated and concentrated along the incident wave direction ($\theta = 0$); 2) the imperfection of the interface can significantly alter both the shape and size of the directivity pattern. Particularly the influence of the dielectric imperfection on the directivity pattern is obvious and should not be ignored (i.e., comparing Fig. 3 to Fig. 4).

Figure 5 presents the scattering cross-section of the scattered shear wave for a perfect interface (dashed lines) and for a compliant and weakly conducting interface $\alpha = 0.1\frac{\mu_1}{R}$, $\beta = 0$ (solid lines). It is observed from Fig. 5 that there are a sequence of maxima and minima for the scattered shear wave when the interface is perfect (dashed lines). We further remark that small high-frequency peaks, which correspond to the resonance scattering, can appear for a perfect interface; whilst large low-frequency peaks, which also correspond to the resonance scattering, can be observed for the insulating and rather compliant imperfect interface. Actually, the observed small high-frequency peaks for a perfect interface (from our model where the shear wave speed in the cylinder is lower than that in the matrix) is in agreement with the results of Liu et al. [24]. The lowest frequency at which the large peak appears for the imperfect interface can be also estimated by treating the cylinder as a rigid body; the natural (or resonance) frequency of the corresponding spring-mass system is estimated to be $k_1R = \sqrt{0.2} = 0.4472$, which is very close to the actual resonance frequency $k_1R = 0.4293$ observed in Fig. 5. We remark that similar approaches were proposed in [8] and [20] to obtain a rough estimation for the lowest resonance frequency. Furthermore, our calculations also show (not presented due to space limits) that the scattering cross-sections for the compliant and insulating interface $\alpha = 0.1\frac{\mu_1}{R}$, $\beta = 0$ are quite different from those for the compliant and equipotential interface $\alpha = 0.1\frac{\mu_1}{R}$, $\gamma = 0$. In other words, the dielectric imperfection also has a significant influence on the scattered cross-sections.

6.2 A circumferentially inhomogeneous interface

In this subsection we consider a circumferentially inhomogeneous interface. We further assume the following special circumferentially inhomogeneous interface

$$\alpha(\theta) = \begin{cases} \alpha_0, & |\theta| < \theta_0/2 \\ 0, & \theta_0/2 < |\theta| \le \pi \end{cases}, \quad \beta(\theta) = \begin{cases} \beta_0, & |\theta| < \theta_0/2 \\ 0, & \theta_0/2 < |\theta| \le \pi \end{cases} \tag{32}$$

where α_0 and β_0 are two nonnegative constants. On the part $|\theta| < \theta_0/2$, the cylinder is imperfectly bonded to the matrix; whilst on the rest part of the interface $\theta_0/2 < |\theta| \le \pi$, the
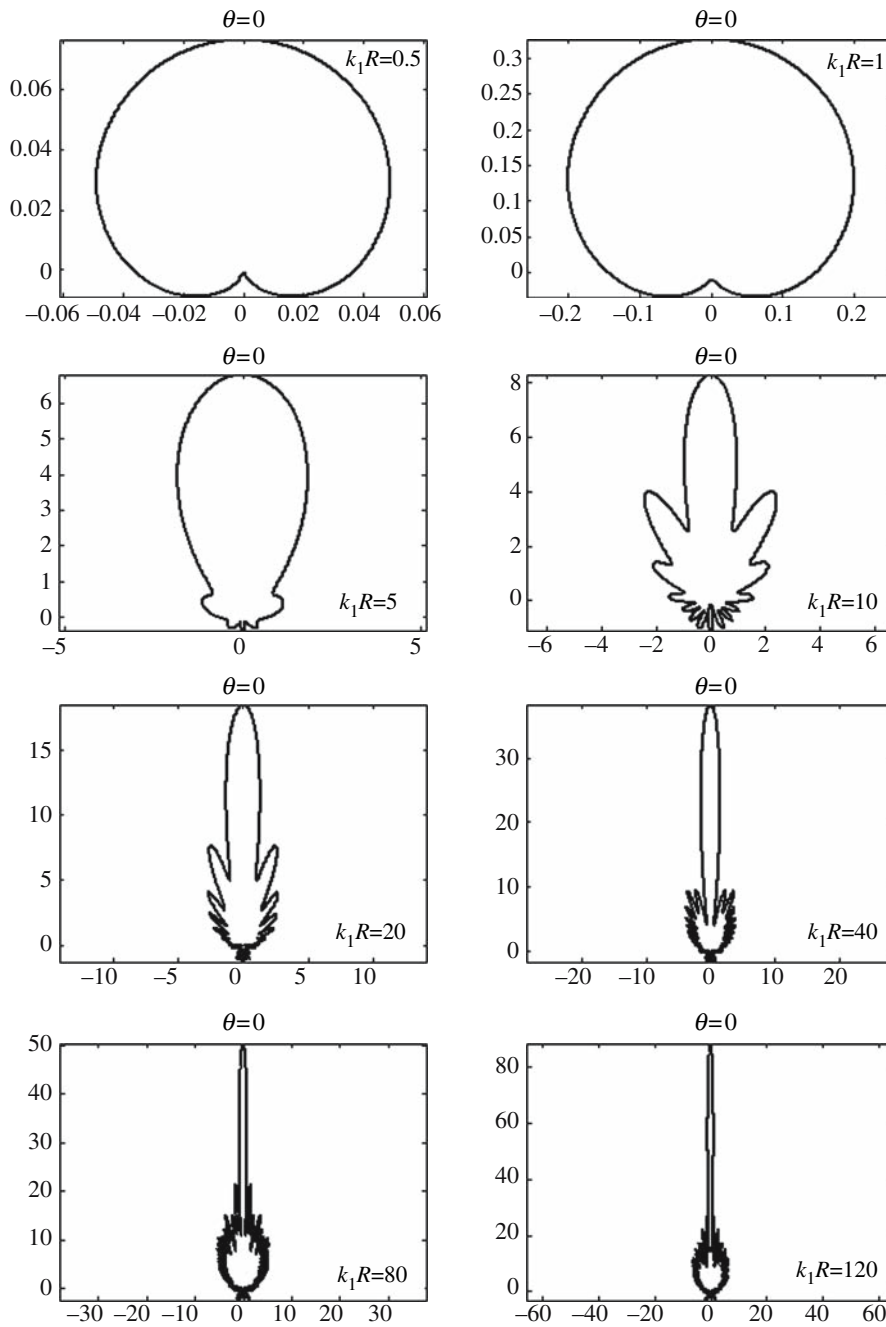
Fig. 2. Directivity patterns of the scattered waves for a perfectly bonded cylinder under eight different frequencies $k_1 R = 0.5,\ 1,\ 5,\ 10,\ 20,\ 40,\ 80,\ 120$

cylinder is completely debonded from the matrix (i.e., this part of the interface is always made of an insulating crack). We further notice that in the limit $\alpha_0, \beta_0 \to \infty$, the inhomogeneous interface model (32) reduces to the partially debonded interface which is made of a perfectly bonded part within $|\theta| < \theta_0/2$ and an insulating crack within $\theta_0/2 < |\theta| \le \pi$.
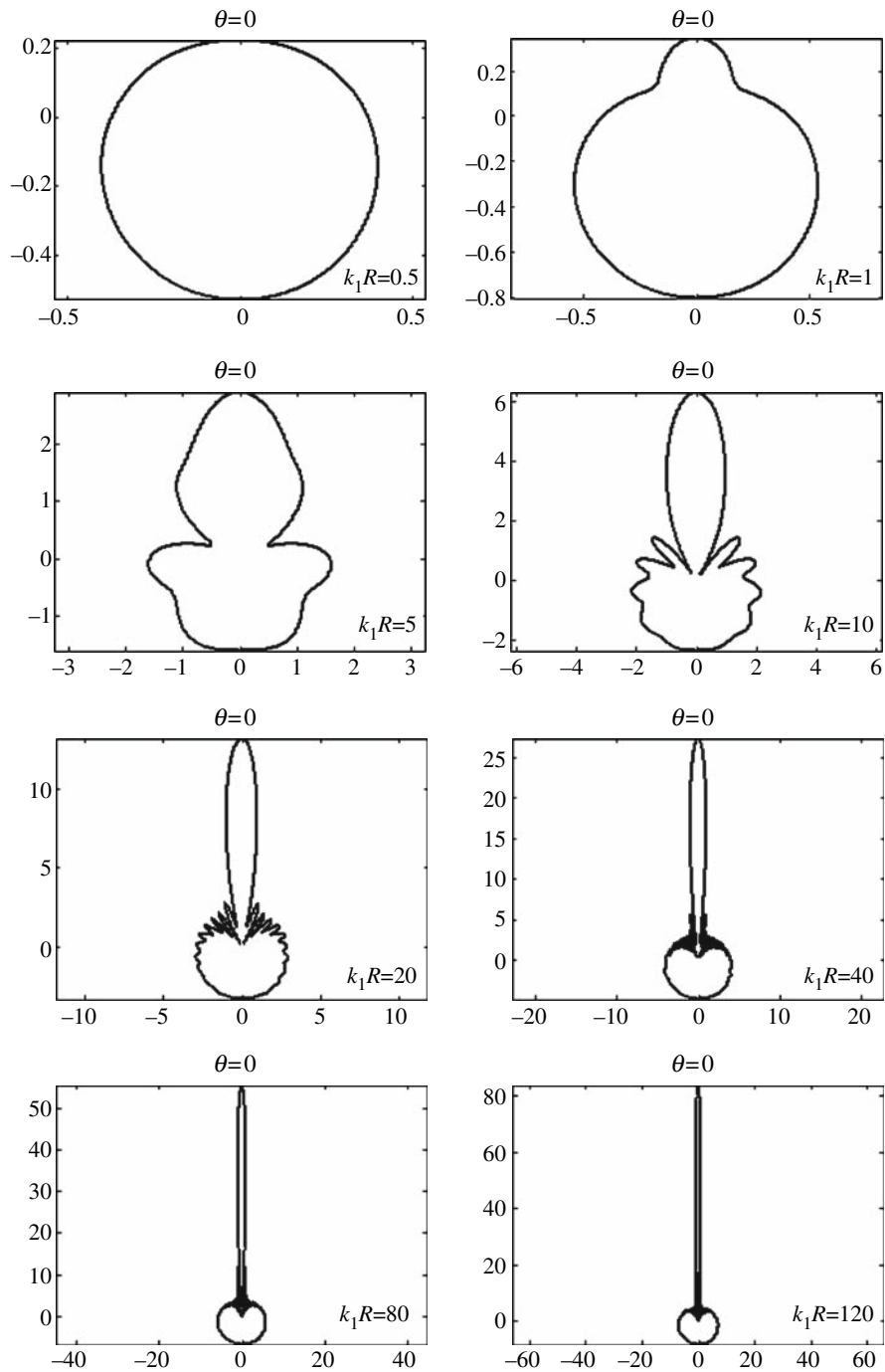
Fig. 3. Directivity patterns of the scattered waves for a cylinder with a compliant and weakly conducting interface $\alpha = 0.1 \frac{\mu_1}{R}$, $\beta = 0.1 \frac{\in_1}{R}$ under eight different frequencies $k_1R = 0.5$, 1, 5, 10, 20, 40, 80, 120
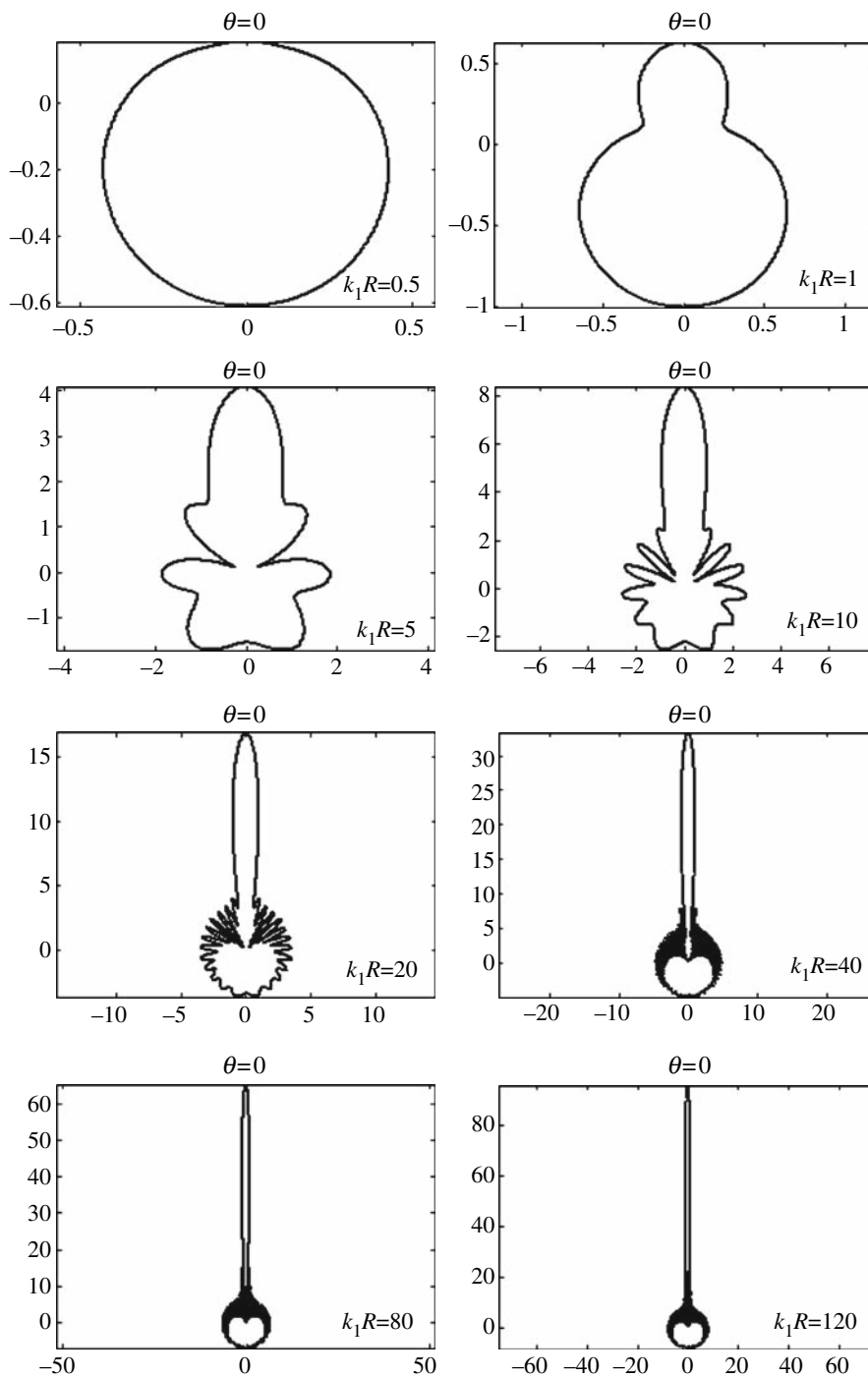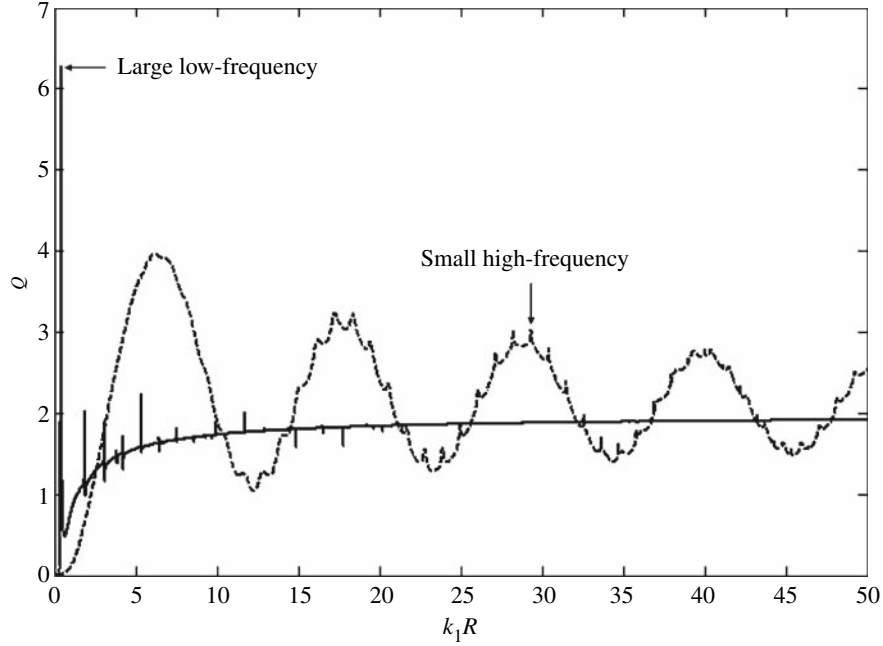
Fig. 4. Directivity patterns of the scattered waves for a cylinder with a compliant and highly conducting interface $\alpha = 0.1\frac{\mu_1}{R}$, $\gamma = \frac{0.1}{\in_1 R}$ under eight different frequencies $k_1R = 0.5$, 1, 5, 10, 20, 40, 80, 120

Fig. 5. Scattering cross-sections of the scattered shear wave for a perfect interface (dashed lines) and for a rather compliant and insulating interface $\alpha = 0.1\frac{\mu_1}{R}$, $\beta = 0$ (solid lines)

The two functions $\alpha(\theta)$ and $\beta(\theta)$ in Eq. (32) can be expanded into Fourier series as

$$\alpha(\theta) = \frac{\alpha_0}{\pi} \sum_{n=-\infty}^{+\infty} \frac{\sin\frac{n\theta_0}{2}}{n} e^{in\theta}, \quad \beta(\theta) = \frac{\beta_0}{\pi} \sum_{n=-\infty}^{+\infty} \frac{\sin\frac{n\theta_0}{2}}{n} e^{in\theta}, \tag{33}$$

where $X_0 = \frac{\alpha_0}{\pi} \lim_{n\to 0} \frac{\sin\frac{n\theta_0}{2}}{n} = \frac{\alpha_0 \theta_0}{2\pi}$, $Y_0 = \frac{\beta_0}{\pi} \lim_{n\to 0} \frac{\sin\frac{n\theta_0}{2}}{n} = \frac{\beta_0 \theta_0}{2\pi}$. In the actual evaluation of Eq. (33), the two Fourier series are truncated at $n = \pm 200$ to obtain results with a relative error less than 0.1%. In order to demonstrate the influence of the inhomogeneity of the interface imperfection, we show in Fig. 6 the directivity patterns for the partially debonded interface which is made of a perfectly bonded part within $|\theta| < \theta_0/2$ and an insulating crack within $\theta_0/2 < |\theta| \le \pi$ ($\alpha_0, \beta_0 \to \infty$) with $k_1 R = 10$. It is observed that the directivity pattern for $\theta_0 = 2\pi$ in Fig. 6 is just that for a perfect interface case as shown in Fig. 2 (for $k_1 R = 10$). Comparing this pattern (corresponding to $\theta_0 = 2\pi$) to the other three cases in Fig. 6, one can clearly observe the significant influence of the interface inhomogeneity on the directivity patterns. It shall be mentioned that due to the nonuniformity of the interface described by Eq. (32), we have to truncate the series in Eqs. (21) and (22) at least at $n = \pm 100$ to obtain results with a relative error less than 1%.

Our formulation is also very convenient to investigate the more general case in which there exist an arbitrary number of cracks along the interface. Let us consider, for instance, m equal-length insulating cracks uniformly distributed along the interface. The rest of the interface is perfectly bonded. The length of each crack is assumed to be $\frac{\pi R}{m}$ (i.e., half of the interface is occupied by cracks), and the centers of these cracks are located at $\theta = \frac{(2j-1)\pi}{m}$, $j = 1, 2, \ldots, m$. Presented in Fig. 7 are the directivity patterns for the case of $m\,(m = 1-8)$ equal-length cracks uniformly distributed along the interface with $k_1 R = 20$. Apparently the number of cracks on the interface greatly affects the shape and size of the directivity patterns. For example when there exists a single crack on the interface ($m = 1$), the magnitudes of the directivity
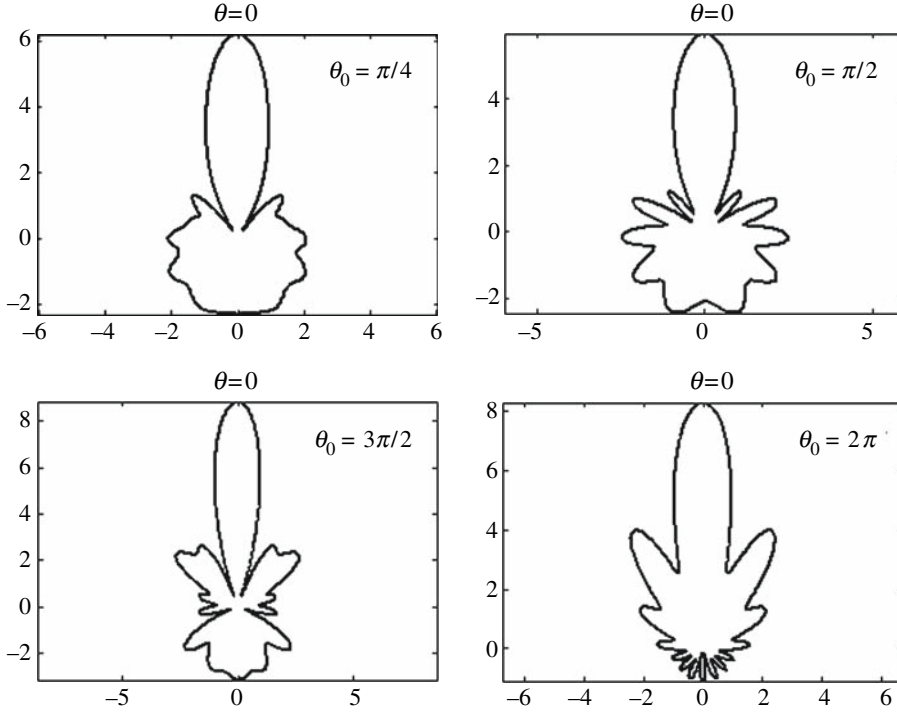
Fig. 6. Directivity patterns of the scattered waves for the partially debonded interface which is made of a perfectly bonded part within $|\theta| < \theta_0/2$ and an insulating crack within $\theta_0/2 < |\theta| \leq \pi$ ($\alpha_0, \beta_0 \to \infty$). The other fixed parameter is $k_1 R = 10$

pattern in the forward ($\theta = 0$ on the top) and backward directions are, respectively, about 16 and 5; while when there are eight cracks on the interface ($m = 8$), these values decrease, respectively, to about 11 and 3. Besides the amplitude, the shape of the directivity patterns for $m = 1$ is also quite different from that for $m = 8$.

Figure 8 demonstrates the scattering cross-sections of the scattered shear wave for a circular cylinder with an imperfect interface described by Eq. (32) with $\alpha_0 = 0.1\frac{\mu_1}{R}$, $\beta_0 = 0$. The large low-frequency peaks are observed for an inhomogeneously imperfect interface. In addition, the resonance frequencies $k_1 R = 0.151, 0.210, 0.295, 0.366, 0.424$ for the five different values of $\theta_0 = \frac{\pi}{4}, \frac{\pi}{2}, \pi, \frac{3\pi}{2}, 2\pi$ observed in Fig. 8 are in close agreement with the predictions $k_1 R = \sqrt{\frac{\theta_0}{10\pi}} = 0.158, 0.224, 0.316, 0.387, 0.447$ by treating the cylinder as a rigid body. It is also clear from Fig. 8 that when θ_0 decreases (i.e., the imperfectly bonded part shrinks and the crack part enlarges), the resonant magnitude of the scattering cross-section increases considerably.

Finally, we present in Fig. 9 the scattering cross-sections of the scattered shear wave for the partially debonded interface which is made of a perfectly bonded part within $|\theta| < \theta_0/2$ and an insulating crack within $\theta_0/2 < |\theta| \leq \pi$ ($\alpha_0, \beta_0 \to \infty$) with $\theta_0 = \pi$ (solid lines) and also for a perfect interface, i.e., $\theta_0 = 2\pi$ (dashed lines). The frequency range is $k_1 R = 0$ to 50. While the shape and size differences of the scattering cross-sections from both the partially debonded and perfectly bonded cylinders can be clearly observed, it is of particular interest to notice that, for a partially debonded cylinder, the resonance peaks exist within the entire frequency domain, spanning from very low to very high frequencies.
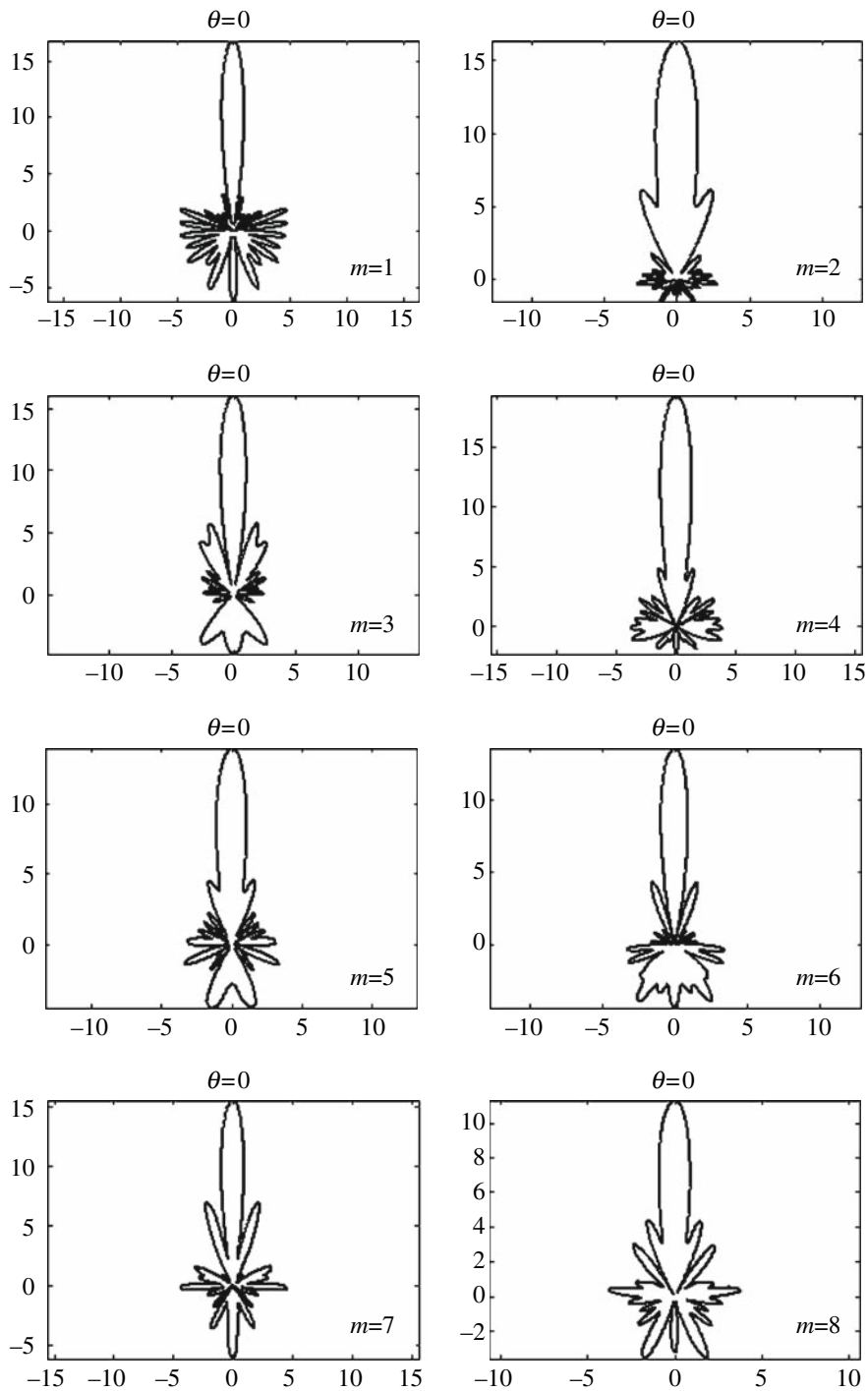
Fig. 7. Directivity patterns of the scattered waves for the case where $m\,(m = 1-8)$ insulating cracks with equal length are uniformly distributed along the interface whilst the rest is perfectly bonded; the other fixed parameter is $k_1 R = 20$
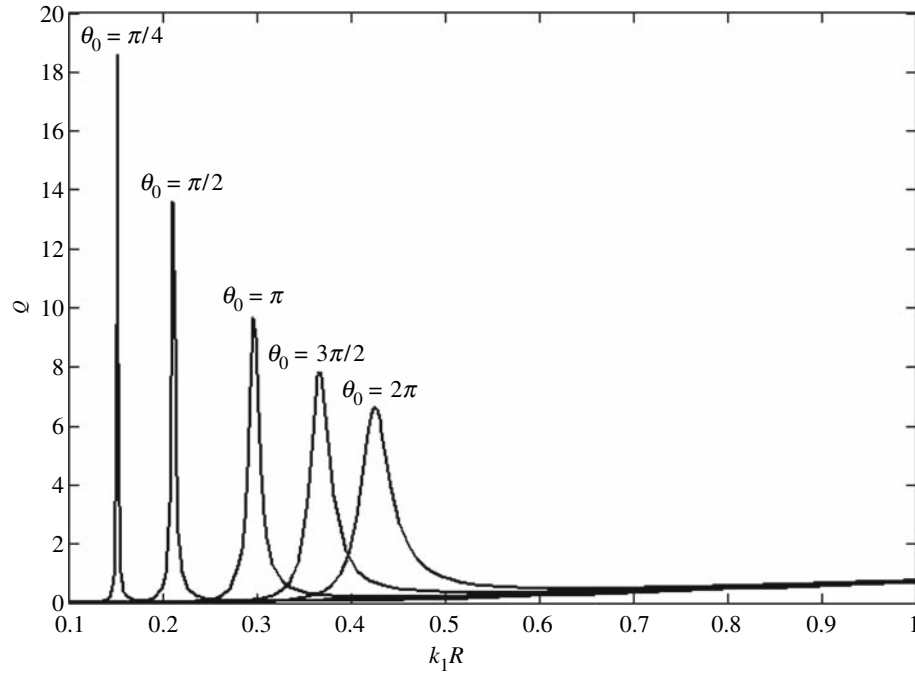
Fig. 8. Scattering cross-sections of the scattered shear wave for a circular cylinder with an inhomogeneous imperfect interface described by Eq. (32) with $\alpha_0 = 0.1\frac{\mu_1}{R}$, $\beta_0 = 0$
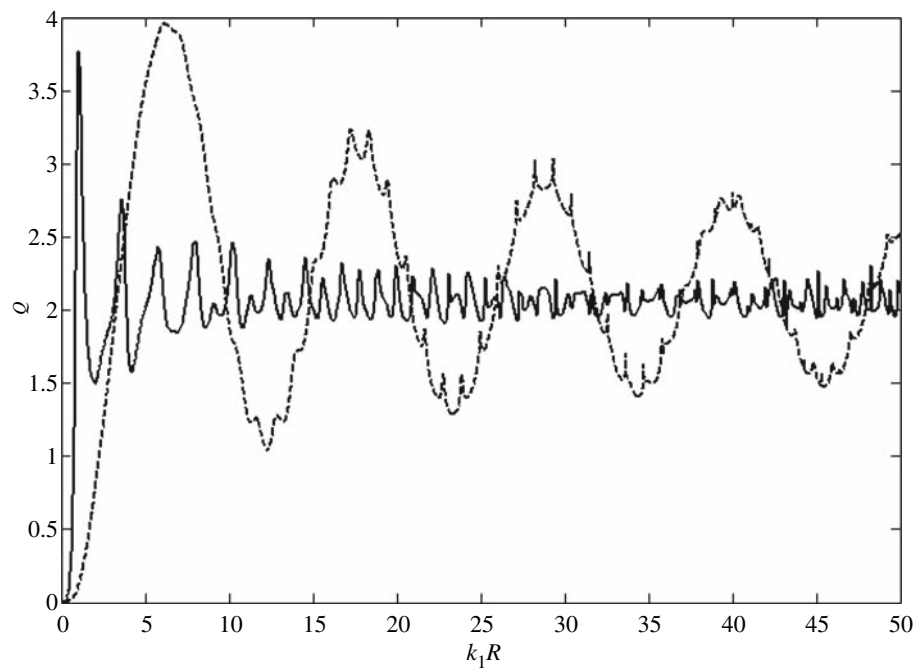

Fig. 9. Scattering cross-sections of the scattered shear wave for the partially debonded interface which is made of a perfectly bonded part within $|\theta| < \theta_0/2$ and an insulating crack within $\theta_0/2 < |\theta| \leq \pi$ ($\alpha_0, \beta_0 \to \infty$) with $\theta_0 = \pi$ (solid lines) and for a perfect interface, i.e., $\theta_0 = 2\pi$ (dashed lines)

7 Conclusions

An exact analysis to the shear wave scattering by an imperfectly bonded piezoelectric cylinder is presented in this paper. Both the homogeneous and circumferentially inhomogeneous imperfect interfaces are considered. The imperfect interface model adopted in this research can be used to simulate damage (e.g., microcracks) occurring on the interface as well as a thin interphase layer between the cylinder and the matrix. Numerical examples demonstrate some distinguished scattering features from homogeneous and inhomogeneous interfaces. The observed large low-frequency peaks of the scattering cross-sections are further verified using the corresponding simplified mass-spring system (by treating the cylinder as a rigid body when the interface is rather compliant). Our numerical results also show clearly the influence of the dielectric imperfection (i.e., weakly conducting and highly conducting) on directivity patterns and scattered cross-sections. While in the present scattering problem, only a single piezoelectric cylinder is considered, the corresponding wave scattering by a cluster of piezoelectric cylinders is also of interest and forms the subject of future study. We point out that the forward solution presented in this paper, combined with the corresponding inverse algorithm, could be very useful to the design of photonic band gap materials where interface imperfection plays an important role [19]–[21].

References

[1] Benveniste, Y.: The effective mechanical properties of composite materials with imperfect contact between the constituents. Mech. Mater. **4**, 197–208 (1984).

[2] Hashin, Z.: The spherical inclusion with imperfect interface. ASME J. Appl. Mech. **12**, 444–449 (1991).

[3] Zhao, Y. H., Weng, G. J.: Plasticity of a two-phase composite with partially debonded inclusions. Int. J. Plast. **12**, 781–804 (1996).

[4] Ru, C. Q., Schiavone, P.: A circular inclusion with circumferentially inhomogeneous interface in antiplane shear. Proc. R. Soc. Lond. A **453**, 2551–2572 (1997).

[5] Wang, X. D., Meguid, S. A.: Dynamic interaction between a matrix crack and a circular inhomogeneity with a distinct interphase. Int. J. Solids Struct. **36**, 517–531 (1999).

[6] Fan, H., Wang, G. F.: Screw dislocation interacting with imperfect interface. Mech. Mater. **35**, 943–953 (2003).

[7] Wang, X., Sudak, L. J., Ru, C. Q.: Elastic field of two imperfectly bonded half-planes with a thermal inclusion of arbitrary shape. ZAMP (2007, in press).

[8] Wang, X., Sudak, L. J.: Scattering of elastic waves by multiple elastic circular cylinders with imperfect interface. Waves Random Media (2007, in press).

[9] Benveniste, Y., Miloh, T.: The effective conductivity of composite with imperfect contact at constituent interfaces. Int. J. Engng. Sci. **24**, 1537–1552 (1986).

[10] Chen, T.: Thermal conduction of a circular inclusion with variable interface parameter. Int. J. Solids Struct. **38**, 3081–3097 (2001).

[11] Fan, H., Sze, K. Y.: A micro-mechanics model for imperfect interface in dielectric materials. Mech. Mater. **33**, 363–370 (2001).

[12] Pan, E.: Mindlin's problem for an anisotropic piezoelectric half space with general boundary conditions. Proc. R. Soc. Lond. A **458**, 181–208 (2002).

[13] Pan, E.: Three-dimensional Green's functions in an anisotropic half space with general boundary conditions. ASME J. Appl. Mech. **70**, 101–110 (2003).

[14] Pan, E.: Three-dimensional Green's functions in anisotropic elastic bimaterials with imperfect interfaces. ASME J. Appl. Mech. **70**, 180–190 (2003).

[15] Pan, E.: Some new three-dimensional Green's functions in anisotropic piezoelectric bimaterials. Electron. J. Bound. Elem. **1**, 236–269 (2003).

[16] Wang, X., Sudak, L. J.: A piezoelectric screw dislocation interacting with an imperfect piezoelectric bimaterial interface. Int. J. Solids Struct. **44**, 3344–3358 (2007).

[17] Fan, H., Yang, J. S., Xu, L. M.: Piezoelectric waves near an imperfectly bonded interface between two half-spaces. Appl. Phys. Lett. **88**, 203–509 (2006).

[18] Cheng, Z. Q., Jemah, A. K., Williams, F. W.: Theory of multilayered anisotropic plates with weakened interfaces. ASME J. Appl. Mech. **63**, 1019–1026 (1996).

[19] Liu, Z., Zhang, X., Mao, Y., Zhu, Y. Y., Yang, Z., Chan, C. T., Sheng, P.: Locally resonant sonic materials. Science **289**, 1734–1736 (2000).

[20] Cai, L. W.: Scattering of antiplane shear waves by layered circular elastic cylinder. J. Acoust. Soc. Am. **115**, 515–522 (2004).

[21] Qi, B., Chen, J. J., Cheng, J. C.: Local resonant characteristics of a layered cylinder embedded in the elastic medium. Chinese Phys. **14**, 2522–2528 (2005).

[22] Miloh, T., Benveniste, Y.: On the effective conductivity of composites with ellipsoidal inhomogeneities and highly conducting interface. Proc. R. Soc. Lond. A **455**, 2687–2706. (1999).

[23] Watson, G. N.: A Treatise on the theory of Bessel functions. Cambridge: Cambridge University Press 1996.

[24] Liu, Y. B., Wu, R. S., Ying, C. F.: Scattering of elastic waves by an elastic or viscoelastic cylinder. Geophys. J. Int. **142**, 439–460 (2000).

[25] Asatryan, A. A., Busch, K., McPhedran, R. C., Botten, L. C., Sterke, C. M., Nicorovici, N. A.: Two-dimensional Green tensor and local density of states in finite-sized two-dimensional photonic crystals. Waves Random Media **13**, 9–25 (2003).

Authors' addresses: X. Wang and E. Pan, Department of Civil Engineering, University of Akron, Akron, OH 44325-3905 (E-mail: pan2@uakron.edu); A. K. Roy, Air Force Research Laboratory, AFRL/MLBCM, Bldg. 654, 2941 Hobson Way, Wright-Patterson AFB, OH 45433-7750